UC San Diego

UC San Diego Previously Published Works

Title

Cation Vacancies Enable Anion Redox in Li Cathodes.

Permalink

https://escholarship.org/uc/item/5hs964cb

Journal

Journal of the American Chemical Society, 146(30)

Authors

Kim, Seong

Kitchaev, Daniil

Patheria, Eshaan

et al.

Publication Date

2024-07-31

DOI

10.1021/jacs.4c05769

Peer reviewed

eScholarship.org Powered by the California Digital Library
University of California

JACS
JOURNAL OF THE AMERICAN CHEMICAL SOCIETY
pubs.acs.org/JACS

Open Access
This article is licensed under CC-BY-NC-ND 4.0

Article

Cation Vacancies Enable Anion Redox in Li Cathodes

Seong Shik Kim, Daniil A. Kitchaev, Eshaan S. Patheria, Colin T. Morrell, Michelle D. Qian, Jessica L. Andrews, Qizhang Yan, Shu-Ting Ko, Jian Luo, Brent C. Melot, Anton Van der Ven, and Kimberly A. See*

Cite This: J. Am. Chem. Soc. 2024, 146, 20951−20962

Read Online

ACCESS | Metrics & More | Article Recommendations | Supporting Information

ABSTRACT: Conventional Li-ion battery intercalation cathodes leverage charge compensation that is formally associated with redox on the transition metal. Employing the anions in the charge compensation mechanism, so-called anion redox, can yield higher capacities beyond the traditional limitations of intercalation chemistry. Here, we aim to understand the structural considerations that enable anion oxidation and focus on processes that result in structural changes, such as the formation of persulfide bonds. Using a Li-rich metal sulfide as a model system, we present both first-principles simulations and experimental data that show that cation vacancies are required for anion oxidation. First-principles simulations show that the oxidation of sulfide to persulfide only occurs when a neighboring vacancy is present. To experimentally probe the role of vacancies in anion redox processes, we introduce vacancies into the Li_2TiS_3 phase while maintaining a high valency of Ti. When the cation sublattice is fully occupied and no vacancies can be formed through transition metal oxidation, the material is electrochemically inert. Upon introduction of vacancies, the material can support high degrees of anion redox, even in the absence of transition metal oxidation. The model system offers fundamental insights to deepen our understanding of structure−property relationships that govern reversible anion redox in sulfides and demonstrates that cation vacancies are required for anion oxidation, in which persulfides are formed.

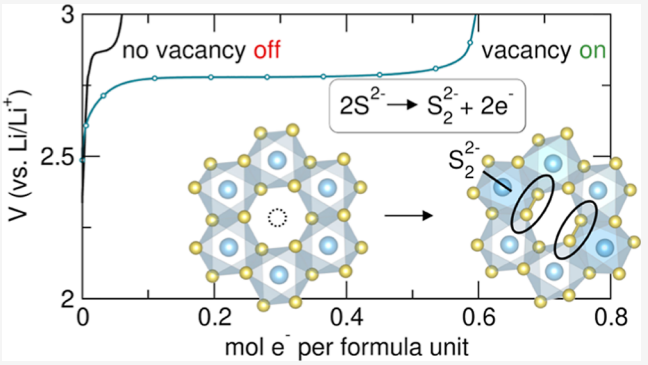

INTRODUCTION

Developments in Li-ion batteries (LIBs) have enabled the modern technological era, and their future applications could have a dramatic impact on sustainability.[1,2] Since the 1990s, LIB cathode chemistry has been dominated by layered transition metal oxides, such as $LiMO_2$, where M is a combination of transition metals. The charge compensation in $LiMO_2$ was largely thought to be localized to the M, but recent works have shown that M, particularly Ni, has larger degree of covalency with O and thus contribution from anion than previously anticipated.[3,4] The intercalation mechanism is quite reversible; however, intercalation materials are reaching their theoretical capacity limits.[5]

To increase the energy density of LIBs, cathode materials capable of storing more than one electron per transition metal, so-called multielectron redox, through the additional redox activity of lattice anions have received increasing attention.[6,7] In Li-rich oxides, the charge compensation has been suggested to involve both the transition metal and the oxide anions. However, the underlying mechanism of multielectron capacity observed in Li-rich oxides remains subject to debate, with proposed mechanisms invoking oxidation of hybridized M−O states[8,9] and various forms of oxidized O.[10,12−19]

To effectively leverage anion redox, design rules controlling the reversible oxidation of anions need to be understood. Here, we aim to probe the effect of cation vacancies in the transition metal layer on anion redox, specifically, their ability to physically accommodate local structural distortions associated with dimer formation. Hong *et al.* suggested that cation vacancies that form as a result of transition metal migration stabilize the formation of short Ir−O π bonds and 1.4 Å O−O dimers through local structural defects that accommodate small distortions in $Li_2Ir_{1-y}Sn_yO_3$.[28] Similarly, House *et al.* recently demonstrated that the loss of Li from the transition metal layer and transition metal migration during charge result in vacancy clusters in $Na_{0.75}(Li_{0.25}Mn_{0.75})O_2$ that accommodate the formation of molecular O_2 in the bulk.[16] The driving force behind the vacancy cluster formation is ascribed to the lower energy of O_2 dimer-containing structure that promotes Mn

Received: April 29, 2024
Revised: July 10, 2024
Accepted: July 10, 2024
Published: July 22, 2024

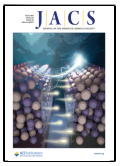

© 2024 The Authors. Published by American Chemical Society

migration to disrupt the honeycomb superstructure.[29] In Li-rich oxides, the formation of cation vacancy clusters is a byproduct of O dimerization that leads to irreversible transition metal migration and voltage hysteresis. In other words, recent studies focusing on Li-rich oxides have suggested the significance of cation vacancies in facilitating anion redox, especially mechanisms that result in structural changes. However, in all cases, the role of cation vacancies has not been experimentally verified. Vacancies have been formed through delithiation with charge compensation on the transition metal or by transition metal migration, making it very difficult to pin down their mechanistic contribution in anion redox.

Here, we aim to probe the effect of vacancies on anion redox by developing model systems that allow us to definitively examine their role. Li-rich oxides suffer from a number of undesirable side reactions that complicate both the development of a mechanistic understanding of anion redox and the practical development of Li-rich cathodes,[19−22] and so we focus on Li-rich sulfides. Unlike Li-rich oxides, anion redox in Li-rich sulfides intrinsically operates at lower voltages due to the higher energy of S p states compared to that of the O p states. Sulfide oxidation in Li-rich sulfides occurs below the potential at which bulk electrolyte decomposition occurs. Furthermore, oxidation of sulfides can lead to the formation of persulfide moieties without breaking the transition metal−S bond.[23] The energetics of the S valence states allow S to form relatively covalent metal−anion bonds with the more abundant, less expensive 3d transition metals. In thermodynamically stable materials, including minerals like pyrite, S exists fully or partially as dimerized $(S_2)^{2-}$ pairs.[24−27] Therefore, persulfides can serve as thermodynamically stable structural features that can promote increased electrochemical activity. Also, studying Li-rich sulfides whose charge compensation mechanism can be precisely characterized allows us to assess the effect of a particular anion redox mechanism on the electrochemical and structural properties. The S K-edge X-ray absorption spectrum can identify not only anion oxidation but also determine if S−S bonds are formed.[30]

We hypothesize that activating S-oxidation *via* persulfide formation requires structural motifs that can accommodate local distortions associated with S−S bond formation. In this work, we target a specific type of defect, cation vacancies, and explore its role in activating S-oxidation. To determine if anion redox is indeed enabled by the presence of vacancies, a material is needed that cannot be electrochemically oxidized during charge when the cation sublattice is fully occupied as a negative control and allows for only anion oxidation when cation vacancies are introduced (Figure 1).

The negative control thus precludes the use of Li-rich materials with open shell transition metals since oxidation will simply form vacancies by virtue of transition metal oxidation and Li^+ delithiation and prevent observation of the negative control case. Here, we use Li_2TiS_3 as the negative control since it has a fully occupied cation sublattice, d^0 Ti^{4+}, and oxidation yields minimal capacity.[24,31−35] We then demonstrate that anion redox is activated in otherwise inert Li_2TiS_3 by introducing cation vacancies while maintaining the Ti oxidation state at Ti^{4+}. We introduce intrinsic vacancies *via* solid-state synthesis by increasing the Ti^{4+}/Li^+ ratio, circumventing complications associated with initial transition metal oxidation. Using spectroscopic techniques and first-principles simulations, we demonstrate that intrinsic cation vacancies in

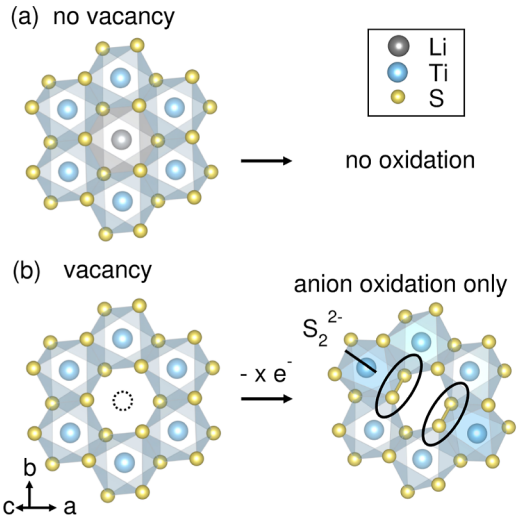

Figure 1. Cartoon representation of a (a) fully occupied cation sublattice in which no oxidation occurs and (b) cation vacancy in the transition metal layer enabling anion redox.

$Li_{1.33-1.33z}Ti_{0.67+0.33z}\square_zS_2$ activate anion redox by allowing for persulfide formation, which is responsible for the observed excess capacity. Thus, we show that cation vacancies are a necessary structural motif to liberate and rehybridize S p orbitals, activating sulfide anion redox.

RESULTS

Mechanism of S Redox in Mixed Valence $Li_{1+x}Ti_{1-x}S_2$.

Previous works have shown that Li_2TiS_3 is electrochemically inactive.[24,31−35] Li_2TiS_3 is similar to $LiTiS_2$ but with 1/3 of the Ti sites in the metal layer substituted by Li to yield a fully occupied cation sublattice and fully oxidized d^0 Ti^{4+}. The structure of $LiTiS_2$ can be described as a layer of edge-sharing octahedrally coordinated Li separated by a layer of edge-sharing octahedrally coordinated Ti. Thus, the stoichiometry of the Li-rich phase can be written as $Li(Li_{1/3}Ti_{2/3})S_2$, where the alkali stoichiometry outside the parentheses indicates the composition of cations in the Li layer and the alkali + metal stoichiometry within the parentheses indicates the composition of the metal layer. Li can also occupy the Ti sites at various ratios, and thus the Li-rich phases can be more generally described as $Li(Li_xTi_{1-x})S_2$.[33]

Using the $Li(Li_xTi_{1-x})S_2$ family of materials as a model system, we first turn to density functional theory (DFT) calculations to probe the correlation between anion oxidation and the vacancy content. Most compositions of $Li(Li_xTi_{1-x})S_2$ contain mixed valence $Ti^{3+/4+}$ and yield Ti^{3+} oxidation commensurate with the formation of Li^+ vacancies. As a representative example of such mixed valence $Ti^{3+/4+}$ compounds analogous to those reported by Flamary-Mespoulie *et al.*,[33] we computationally examine the oxidation of $Li(Li_{1/9}Ti_{8/9})S_2$, which can be written as $[Li_9][Li_1Ti_6^{3+}Ti_2^{4+}]S_{18}$. We assume that this compound is layered, consistent with the $R\bar{3}m$ space group reported experimentally, with a representative Li−Ti arrangement in the Ti layer, as shown schematically in Figure 2a. Figure 2b shows calculated formation energies of enumerated configurations of this compound as Li is extracted for three scenarios: (a) $Ti^{3+/4+}$ oxidation followed by on-lattice S-oxidation with no persulfide formation ($0S_2^{2-}$), (b) $Ti^{3+/4+}$ oxidation followed by the formation of one persulfide ($1S_2^{2-}$), or (c) $Ti^{3+/4+}$ oxidation

https://doi.org/10.1021/jacs.4c05769
J. Am. Chem. Soc. 2024, 146, 20951−20962

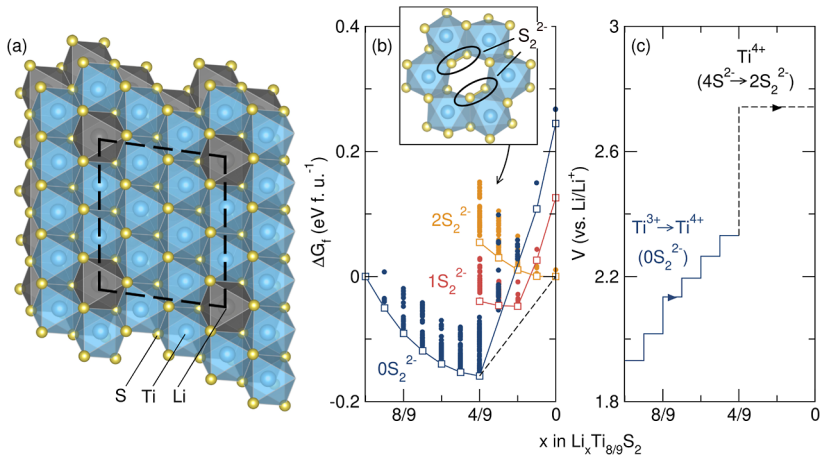

Figure 2. (a) Structure of model $Li(Li_{1/9}Ti_{8/9})S_2$ compound viewed down the *c*-axis onto the transition metal layer. (b) Thermodynamic enumeration of delithiated states illustrating the relative energies of $Ti^{3+/4+}$ oxidation, on-lattice S-oxidation ($0S_2^{2-}$), and S-oxidation through the formation of persulfides ($1S_2^{2-}$ and $2S_2^{2-}$). (c) Voltage curve corresponding to the equilibrium persulfide pathway on charge.

followed by the formation of two persulfides ($2S_2^{2-}$). The formation of two persulfides at full delithiation is the lowest energy pathway, while on-lattice S-redox ($0S_2^{2-}$) is substantially higher in energy. The corresponding voltage curve shown in Figure 2c reveals close agreement with the experimental data reported by Flamary-Mespoulie *et al.*,[33] with a sloping voltage profile in the $Ti^{3+/4+}$ region and a jump to ≈2.8 V at the onset of S-oxidation.

A critical feature of the redox mechanism proposed in Figure 2 is that the low-energy persulfide pathway is possible only in the presence of a cation vacancy in the Ti-layer. Persulfide formation requires a distortion of the local environment, which in the absence of a vacancy is structurally unfavorable. However, on-lattice S-oxidation is a high-energy process that requires much higher voltages than those observed experimentally and is unlikely to be observable in practice. In fact, upon charging Li_2TiS_3 to higher voltages, no additional capacity is observed prior to bulk electrolyte decomposition (Figure S23). We thus propose that the reason Li_2TiS_3 is electrochemically inactive is the insufficient amount of vacancies in the material, which suppresses the formation of persulfides responsible for the S-redox activity.

Introduction of Vacancies by Substitution. Based on the proposed vacancy-mediated mechanism in the mixed-valence compounds, we hypothesize that pure S-redox can be activated in Li_2TiS_3 by chemically introducing vacancies into the pristine material. Vacancies can be introduced by the aliovalent substitution of Ti for Li in Li_2TiS_3. During synthesis, for every additional Ti^{4+}, four Li^+ are removed to maintain the Ti oxidation state at Ti^{4+}, yielding a general stoichiometry of $Li_{1.33-1.33z}Ti_{0.67+0.33z}\square_zS_2$, where □ = vacancy and *z* = vacancy content. Li_2TiS_3 will be described hereafter as $Li_{1.33}Ti_{0.67}S_2$ for the sake of consistency.

Compounds with various vacancy contents are synthesized in the form $Li_{1.33-1.33z}Ti_{0.67+0.33z}\square_zS_2$. Excess S (+0.1 mol) must be used during synthesis to maintain a partial pressure of S in the headspace of the reaction ampule and drive the formal oxidation state of Ti closer to Ti^{4+}. We chose $LiTi_{0.75}\square_{0.25}S_2$ for in-depth analysis based on its superior electrochemical performance (*vide infra*). The synchrotron X-ray diffraction (sXRD) pattern and quantitative Rietveld refinement of $LiTi_{0.75}\square_{0.25}S_2$ are shown in Figure 3a (see Figure S1 for XRD patterns of $Li_{1.33-1.33z}Ti_{0.67+0.33z}\square_zS_2$). The pattern can be refined to a single phase in the O3 $R\bar{3}m$ space group, as opposed to the lower symmetry $C2/m$ space group of the parent phase $Li(Li_{1/3}Ti_{2/3})S_2$, due to a lack of honeycomb ordering within the Ti/Li layer. The lattice parameters of $LiTi_{0.75}\square_{0.25}S_2$ are a = 3.525 Å and c = 18.066 Å, which show that the phase is slightly contracted in the a direction and expanded in the c direction upon vacancy introduction. Minor impurities observed in the low Q region between 1.6 and 3.1 Å^{-1} are fit to elemental S_8 with 0.0015 phase fraction, or 1.9 wt %, which do not appear when stoichiometric S is used in the synthesis (Figure S2). The presence of S_8 is attributed to the excess S used in the solid-state synthesis to ensure full oxidization of Ti and full occupation of the anion sublattice. When the occupancy of Ti and S is refined in the Rietveld refinement of sXRD patterns of pristine $LiTi_{0.75}\square_{0.25}S_2$, the occupancy refines to 0.79 and 1.02 for Ti and S, respectively, further supporting that the Ti layer is not fully dense (Figure S3). Transmission electron microscopy (TEM) images are indexed to the $R\bar{3}m$ space group and reveal a layered structure free of Ti in the Li layer, confirming that additional Ti is incorporated only into the Ti/Li layer (Figure S4).

To confirm the stoichiometry of the material, elemental analysis is undertaken with electron probe microanalysis (EPMA). EPMA is a wavelength-based technique that yields elemental ratios 30−40 times more quantitative than those obtained with energy-dispersive spectroscopy (EDS).[36,37] A table summarizing the EPMA results and more information can be found in Supporting Note 1. $LiTi_{0.75}\square_{0.25}S_2$ prepared with Li_2S, synthesized (stoichiometric) TiS_2, and 0.1 excess S exhibits a Ti/S ratio of 1:2.67, showing good agreement with the theoretical ratio.

The Li/Ti ratio in $LiTi_{0.75}\square_{0.25}S_2$ is probed with inductively coupled plasma mass spectrometry (ICP−MS). We note that S is precluded in the ICP−MS analysis due to its volatility in the solvent, which results in inaccurate elemental composition. The Li/Ti ratio obtained from ICP−MS is 1:0.733 ± 0.006, which is very close to the target Li/Ti ratio of 1:0.75. Taking the Ti/S ratio from EPMA and the Li/Ti ratio from ICP−MS, the stoichiometry of the synthesized material is $Li_{1.02}Ti_{0.75}\square_{0.23}S_2$ to give a total cation content of 1.77 mol per f.u. thereby confirming the presence of cation vacancies in the material. Because the stoichiometry is so close to the input

https://doi.org/10.1021/jacs.4c05769
J. Am. Chem. Soc. 2024, 146, 20951−20962

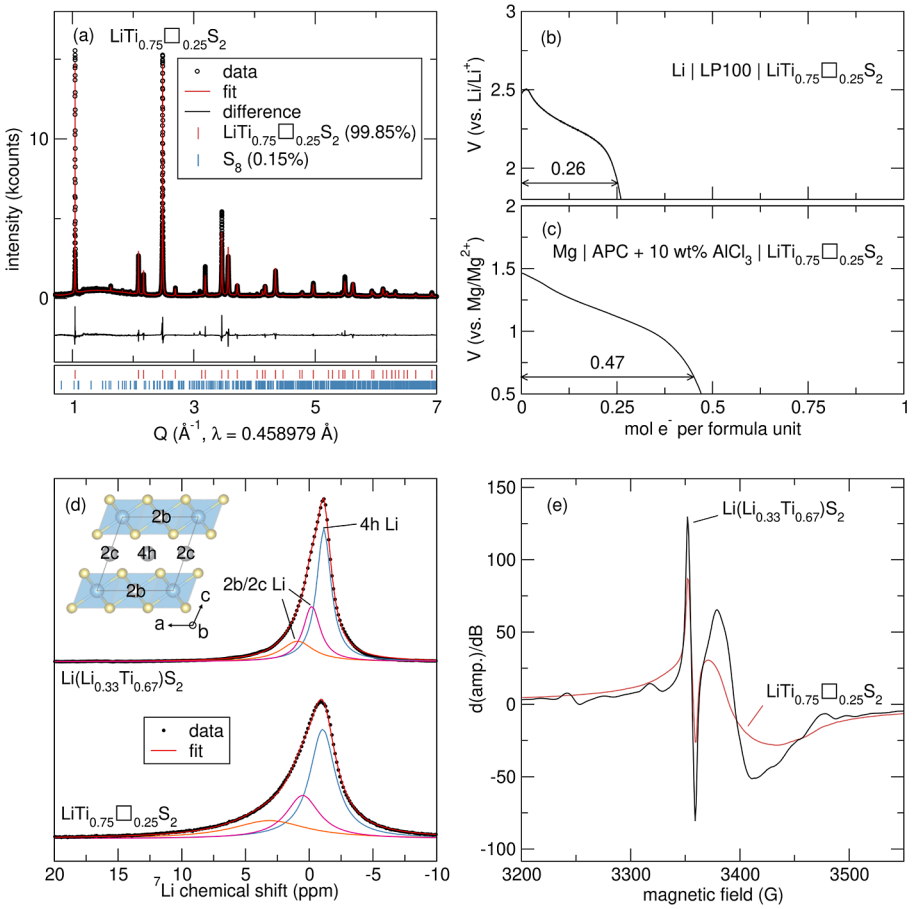

Figure 3. (a) Synchrotron powder XRD patterns with quantitative Rietveld refinements of $LiTi_{0.75}\square_{0.25}S_2$ with a two-phase fit to 99.85% $LiTi_{0.75}\square_{0.25}S_2$ and 0.15% S_8. The tick marks indicate the Bragg reflection positions with the space group $R\bar{3}m$ with 0.15% S_8 impurities. Discharge curves of $LiTi_{0.75}\square_{0.25}S_2$ (b) at room temperature and C/500 based on 1 e^- per formula unit in a Li electrolyte and (c) at 60 °C and C/100 based on 1 e^- per formula unit in a Mg electrolyte. The discharge capacities suggest a vacancy concentration of 0.26 and 0.24, respectively. The apparent vacancy concentration is slightly lower when using a Mg^{2+} working ion, likely due to kinetic limitations which may prevent occupation of every vacancy. (d) ^{7}Li MAS ssNMR spectra of pristine $Li(Li_{1/3}Ti_{2/3})S_2$ and $LiTi_{0.75}\square_{0.25}S_2$ collected at 13 kHz. Both spectra are fit with 3 components, signifying that vacancies are not exclusively formed in the Ti layer. (e) EPR spectra of pristine $Li(Li_{1/3}Ti_{2/3})S_2$ and $LiTi_{0.75}\square_{0.25}S_2$, suggesting a small concentration of Ti^{3+} in both materials.

stoichiometry, we will continue to use the target stoichiometry throughout the rest of the paper.

With the Li/Ti and Ti/S ratios of $LiTi_{0.75}\square_{0.25}S_2$ confirmed by ICP–MS and EPMA, the vacancy content can be further probed electrochemically, using the fact that the material can be reduced to incorporate a mobile ion into cation vacancies. Figure 3b depicts galvanostatically discharged $LiTi_{0.75}\square_{0.25}S_2$ in a Li electrolyte. When $LiTi_{0.75}\square_{0.25}S_2$ is discharged at a very slow rate of C/500, a discharge capacity of 0.26 mol e^- per formula unit (f.u.) is observed, which is in good agreement with the targeted vacancy content of 0.25 mol per f.u. To further confirm the vacancy concentration, we discharge the material with a Mg electrolyte to incorporate a divalent cation. Mg^{2+} can occupy the octahedral sites in layered TiS_2.[38] The discharge curve in a Mg electrolyte is shown in Figure 3c. With a Mg^{2+} working ion, we measure a capacity of 0.47 mol e^- per f.u., which would indicate a vacancy concentration of 0.24 mol per f.u. (see Figure S5 for replicates).

Next, solid-state nuclear magnetic resonance (ssNMR) spectroscopy is employed to probe the location of the vacancies indirectly by characterizing the local Li environments. ^{7}Li magic-angle spinning (MAS) ssNMR spectra of $Li(Li_{1/3}Ti_{2/3})S_2$ and $LiTi_{0.75}\square_{0.25}S_2$ are shown in Figure 3d. The ^{7}Li MAS spectrum of the parent phase $Li(Li_{1/3}Ti_{2/3})S_2$ is fit with three components (Figure 3d), consistent with previously reported isostructural materials Li_2TiSe_3 and Li_2TiO_3, representing the two unique Li environments in the Li layer (2*c* and 4*h*) and one Li environment in the Ti/Li layer (2*b*).[34,39,40] The relative areas of the components are determined based on the ratio of the Wyckoff site multiplicity of each Li site. Based on the relative intensities, we assign the most intense peak to the 4*h* Li site. We cannot decouple the remaining 2*b* and 2*c* Li sites, as their multiplicities are identical. The resonance broadens with an increasing vacancy content (Figure S6), suggesting increased disorder. The ^{7}Li MAS spectrum of $LiTi_{0.75}\square_{0.25}S_2$ is fit to 3 components analogously to $Li(Li_{1/3}Ti_{2/3})S_2$ (Figure 3d, see Figure S7 for 2-component fit). Because all three chemical environments are still present in $LiTi_{0.75}\square_{0.25}S_2$, Li still occupies each Wyckoff site in the material. If all vacancies were present in the Ti/Li layer in $LiTi_{0.75}\square_{0.25}S_2$, there would be no Li in the Ti/Li layer, and thus either the 2*b* or 2*c* peak would completely disappear. Therefore, vacancies are formed either exclusively in the Li layer or in both the Li and Ti/Li layers. This result is further corroborated by computations that suggest that all low energy configurations of the pristine compound favor vacancy

https://doi.org/10.1021/jacs.4c05769
J. Am. Chem. Soc. 2024, 146, 20951−20962

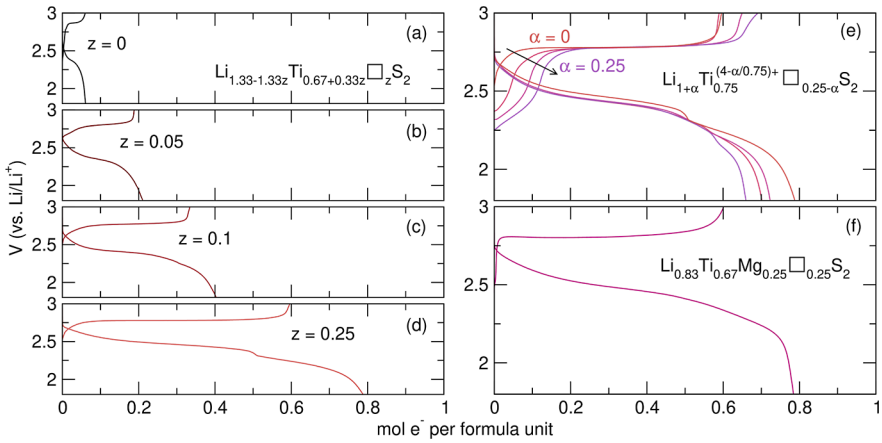

Figure 4. First charge and discharge curves of (a–d) $Li_{1.33-1.33z}Ti_{0.67+0.33z}\square_zS_2$ up to $z = 0.25$ cycled at C/20. Charge capacity is observed upon introduction of vacancies. (e) First charge and discharge curves of $Li_{1+\alpha}Ti_{0.75}\square_{0.25-\alpha}S_2$ cycled at C/20 demonstrating that contributions in the initial sloping region increase with decreasing formal oxidation state of Ti. (f) First charge and discharge curves of $Li_{0.83}Ti_{0.67}Mg_{0.25}\square_{0.25}S_2$ cycled at C/50 showing activation of the material upon vacancy introduction through introduction of Mg^{2+}.

formation in the Li layer (Figure S8). We note that low-field, variable temperature, and ^{6}Li MAS ssNMR cannot resolve the broadened peaks (Figures S9 and S10).

Next, electron paramagnetic resonance (EPR) is used to investigate local electronic environments in $LiTi_{0.75}\square_{0.25}S_2$ and confirm that vacancy introduction does not alter the Ti electronic structure. Figure 3e depicts the EPR spectra of $Li(Li_{1/3}Ti_{2/3})S_2$ and $LiTi_{0.75}\square_{0.25}S_2$ collected at 77 K. Aside from small impurities in $Li(Li_{1/3}Ti_{2/3})S_2$, both spectra are characterized by a sharp feature at $g = 2.02$ and a broader feature at $g = 1.99$. The sharp feature at $g = 2.02$ is observed when electrons are localized in anion vacancies like those in TiO_2 and MoS_2, suggesting that some S vacancies are present in the structure.[41−43] The broader feature at $g = 1.99$ indicates the presence of Ti^{3+}, which also has been observed in other reports of $Li(Li_{1/3}Ti_{2/3})S_2$.[34,35] The presence of the Ti^{3+} feature in both $Li(Li_{1/3}Ti_{2/3})S_2$ and $LiTi_{0.75}\square_{0.25}S_2$ suggests that there is a residual amount of Ti^{3+} in both materials, and forming completely d^0 Ti^{4+} is extremely difficult even with careful precursor tuning. Indeed, Ti-rich $LiTi_{0.75}\square_{0.25}S_2$ and $Li_{1.25}Ti_{0.75}S_2$, materials containing Ti^{3+} based on electrochemical characterization (*vide infra*), exhibit much larger Ti^{3+} features suggesting that the amount of Ti^{3+} in $Li(Li_{1/3}Ti_{2/3})S_2$ and $LiTi_{0.75}\square_{0.25}S_2$ is very small (Figure S11). The similarity between the EPR spectra of $Li(Li_{1/3}Ti_{2/3})S_2$ and those of $LiTi_{0.75}\square_{0.25}S_2$ indicates that vacancy introduction does not alter the local electronic environments.

Impact of Vacancies on the Electrochemical Activity. The effect of cation vacancies in $Li_{1.33-1.33z}Ti_{0.67+0.33z}\square_zS_2$ on the electrochemistry is examined with galvanostatic cycling. The galvanostatic cycling data for $Li_{1.33-1.33z}Ti_{0.67+0.33z}\square_zS_2$ are shown in Figure 4a–d. All cells are charged first, corresponding to oxidation at the cathode. The parent material $Li(Li_{1/3}Ti_{2/3})S_2$ exhibits a minimal capacity of 0.05 e^- per f.u. (Figure 4a), consistent with previous reports.[33,34] With increasing vacancy content, the charge capacity increases reaching 0.6 e^- per f.u. in $LiTi_{0.75}\square_{0.25}S_2$ (Figure 4b–d). All materials exhibit a single plateau in the charge profiles around 2.77 V, consistent with the calculated voltage for S-oxidation (Figure 2c). A single plateau above 2.5 V in other Li-rich sulfides has been attributed to S-oxidation.[24,44,45] Galvanostatic intermittent titration technique (GITT) of $Li_{1.33}Ti_{0.67}S_2$ shows minimal oxidation with an equilibrium V of 2.65 V (Figure S12). Also, discharge capacities are higher than charge capacities for all vacancy contents (Figure 4a–d). Cation vacancies allow more Li^+ to be inserted into the structure than was removed during charge. Although the d^0 electron configuration of Ti^{4+} prevents it from partaking in oxidation, Ti^{4+} can act as an additional reduction center during discharge.

The shape of the curves can indicate the charge compensation mechanism, distinguishing S-oxidation from Ti-oxidation. For instance, Flamary-Mespoulie *et al.* charged $Li_{1.25}Ti_{0.75}S_2$, which has an average formal oxidation state of $Ti^{3.67+}$, and observed first a sloping region below 2.5 V, followed by a plateau around 2.7 V.[33] The two regions were assigned to Ti^{3+} oxidation and S-oxidation, respectively.[33] Therefore, the absence of the sloping region in $Li_{1.33-1.33z}Ti_{0.67+0.33z}\square_zS_2$ suggests no contribution from Ti^{3+} on charge.

To confirm that the sloping region appears when Ti^{3+} is oxidized, we systematically varied the formal oxidation state of Ti by maintaining the Ti stoichiometry at $Ti_{0.75}$ and filling the vacancies with Li^+. The substitution is carried out by increasing the Li content of the precursors during synthesis to yield $Li_{1+\alpha}Ti_{0.75}\square_{0.25-\alpha}S_2$ (see Figure S13 for XRD patterns). Assuming that the excess Li^+ is charge compensated by Ti reduction, the Ti oxidation state will decrease as Li^+ is introduced. Indeed, as Li^+ is introduced, we observe a systematic increase in the capacity from the sloping region (Figure 4e), suggesting that the formal oxidation state of Ti decreases from Ti^{4+} to $Ti^{3.67+}$ (see Figure S14 for individual cycling data). Furthermore, if $LiTi_{0.75}\square_{0.25}S_2$ (formally Ti^{4+}) is discharged first to reduce Ti^{4+}, a sloping region is again observed in the subsequent charge (Figure S15).

To confirm that the introduction of vacancies activates anion oxidation, we targeted an additional method to introduce vacancies. Vacancies are introduced through aliovalent substitution of Mg^{2+} for Li^+ *via* solid-state synthesis to yield $Li_{0.83}Ti_{0.67}Mg_{0.25}\square_{0.25}S_2$ while maintaining the $R\bar{3}m$ space group (Figure S16). Galvanostatic cycling data of $Li_{0.83}Ti_{0.67}Mg_{0.25}\square_{0.25}S_2$ is shown in Figure 4f. The charge capacity is substantial, reaching 0.6 e^- per f.u. Similar to $LiTi_{0.75}\square_{0.25}S_2$, only one plateau is observed in the charge profile, and the discharge capacity is higher than the charge

https://doi.org/10.1021/jacs.4c05769
J. Am. Chem. Soc. 2024, 146, 20951−20962

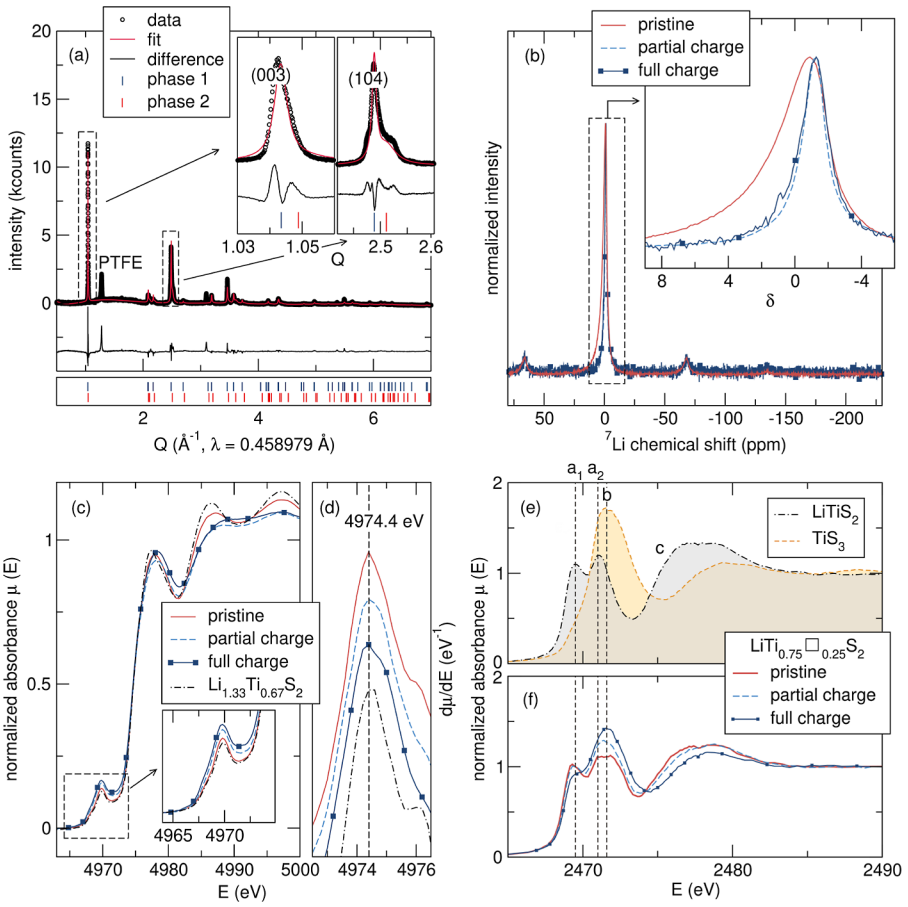

Figure 5. (a) sXRD of fully charged $LiTi_{0.75}\square_{0.25}S_2$ fit to two phases in the $R\bar{3}m$ space group with insets highlighting the (003) and (104) reflections. (b) *Ex situ* ^{7}Li MAS ssNMR of pristine, partially charged, and fully charged $LiTi_{0.75}\square_{0.25}S_2$ with the inset highlighting the central transition. (c) Ti K-edge XANES of $Li(Li_{1/3}Ti_{2/3})S_2$ and $LiTi_{0.75}\square_{0.25}S_2$ at various states of charge and the (d) first derivative of the rising edge. The dashed line represents the peak position of the pristine state. S K-edge XANES of (e) $LiTiS_2$ and TiS_3 standards and (f) $LiTi_{0.75}\square_{0.25}S_2$ at various states of charge.

capacity. It is notable that Mg substitution also activates anion oxidation because Mg substitution does not affect the electronic states near the Fermi level, leaving only the effect of vacancies.

Structural and Spectroscopic Characterization of the Oxidized Material. Next, we characterized the physical and electronic structures of charged $LiTi_{0.75}\square_{0.25}S_2$. We note that detailed analysis on the discharge mechanism is outside the scope of this paper and will be the subject of future studies. First, we investigate the structural evolution of $LiTi_{0.75}\square_{0.25}S_2$ during charge. *Operando* XRD reveals new features upon oxidation, including shoulders on the (003) and (104) reflections (Figure S17), consistent with a two-phase mechanism upon charge, which is also reflected in the flat plateau of the charge profile and the DFT-predicted mechanism.

To get more quantitative information, we turn to the *ex situ* sXRD data of charged $LiTi_{0.75}\square_{0.25}S_2$ depicted in Figure 5a. The sXRD pattern cannot be described with a single phase. Fitting the data to two phases in the $R\bar{3}m$ space group yields reasonable fits; however, some features such as line shape are not well described, and the reflection at approximately 3 Å is not fit. Because the pattern can be relatively well described by structures related to the parent phase, we suggest that no substantial structural rearrangements have occurred. The most complex changes in peak shape are observed in (102) and (104) reflections, which are both dictated by the S sublattice (Figure S18), suggesting that S atoms deviate from the original lattice position as a result of local structural distortions as would be required by formation of persulfides. The (104) reflection is highlighted in Figure 5a due to its higher intensity [see Figure S19 for both the (102) and (104) reflections].

Next, changes in the Li environments are probed by ^{7}Li MAS ssNMR. Figure 5b depicts *ex situ* ^{7}Li MAS ssNMR spectra of $LiTi_{0.75}\square_{0.25}S_2$ at three different states of charge: pristine, partial charge (0.25 e^- removed), and full charge (0.60 e^- removed).

The pristine spectrum is the same as that shown in Figure 3e. After partial charge, the ^{7}Li MAS NMR spectrum loses intensity in the region associated with the 2*b* and 2*c* Li sites, suggesting that most of the remaining Li resides in the 4*h* Li site in the Li layer. In fact, the spectrum is well described by one single component, suggesting that Li is no longer occupying the site in the metal layer (Figure S20). After full charge, the shape of the resonance shows minimal changes, suggesting that Li is removed only from the 4*h* Li site (in the Li layer), causing a decrease in the resonance intensity but no shape change. Again, the resonance can be fit by one single component substantiating the assignment of the partially charged material. Thus, upon oxidation, Li originally present in the Ti/Li layer migrates to the Li layer during delithiation, creating vacancies in the Ti/Li layer.

https://doi.org/10.1021/jacs.4c05769
J. Am. Chem. Soc. 2024, 146, 20951−20962

To probe the role of Ti in the charge compensation mechanism during charge, *ex situ* Ti K-edge X-ray absorption spectroscopy (XAS) is measured at the same states of charge as those measured for ssNMR. Ti K-edge XANES data are plotted in Figure 5c. Ti XANES data of the standards are shown in Figure S21. The rising edge position of pristine $LiTi_{0.75}\square_{0.25}S_2$ at 4974.4 eV aligns with that of $Li(Li_{1/3}Ti_{2/3})S_2$, indicating that the introduction of vacancies does not alter the oxidation state of Ti (Figure 5c). In the spectra of the partially charged and fully charged $LiTi_{0.75}\square_{0.25}S_2$, the rising edge does not shift (Figure 5d), indicating that Ti is not oxidized. The pre-edge peak is attributed to the 1s to 3d transition, which is dipole forbidden for absorbers in a centrosymmetric environment.[46,47] The presence of the pre-edge feature suggests slightly distorted TiS_2 octahedra similar to TiS_2.[47] The pre-edge increases in intensity (Figure 5c inset) during charge, suggesting increased local distortions of TiS_6 octahedra.

The absence of an edge shift in Ti K-edge XANES suggests that Ti does not participate in oxidation throughout charge. DFT calculations illustrate that S-oxidation through the formation of persulfides is more thermodynamically favorable than that through oxidized S holes. In fact, the calculated voltage for S^{2-} oxidizing to S_2^{2-} (2.74 V) matches the experimentally measured voltage of the plateau when $LiTi_{0.75}\square_{0.25}S_2$ is oxidized (2.76 V). To probe the role of S during oxidation, S K-edge XANES is measured on standards and on $LiTi_{0.75}\square_{0.25}S_2$ at the same states of charge measured for the Ti K-edge. First, we will discuss the shape of the S K-edge XANES for two standards shown in Figure 5e: $LiTiS_2$ and TiS_3. The structure of $LiTiS_2$ contains octahedrally coordinated Ti^{3+} with all of the S^{2-} species. The S K-edge spectrum shows two distinct pre-edge features, labeled a_1 and a_2, that result from the electronic transition from the S 1s to 3p σ^* mixed with empty Ti 3d t_{2g} and e_g orbitals, respectively.[30,47−50] TiS_3 contains highly distorted 8-coordinate Ti^{4+} bound to both S^{2-} and S_2^{2-} species. The pre-edge feature in TiS_3 is shifted to higher energy relative to the $LiTiS_2$ pre-edge features due to the hybridization of 3p orbitals to form S_2^{2-} species, which destabilizes the 3p σ^*.[30]

Now, we discuss the *ex situ* S K-edge XANES data of $LiTi_{0.75}\square_{0.25}S_2$ shown in Figure 5f. The pristine $LiTi_{0.75}\square_{0.25}S_2$ shows two features in the pre-edge region, similar to those of the $LiTiS_2$. The a_1 feature lines up well with that measured in $LiTiS_2$. The a_2 feature, however, is much broader because of the small S_8 impurity in the sample. The intensity of this transition is very strong in S_8,[30] so even a small impurity will likely show up in the XAS. Excess S_8 is used in synthesis to drive full oxidation of Ti. Upon oxidation, we observe an increase in the spectral intensity in the region associated with S_2^{2-}, feature b. Furthermore, the intensity of the a_1 and a_2 pre-edges decreases, which would be expected if S^{2-} is being converted to S_2^{2-}. In TiS_2, the decrease in the intensity of t_{2g} and e_g states during reduction is attributed to the partial filling of Ti 3d states and thus the reduced transition probability of S 1s to these levels.[47] In $LiTi_{0.75}\square_{0.25}S_2$, however, the formal oxidation state of Ti remains as 4+ during oxidation, as evidenced by Ti K-edge XANES eliminating such a scenario. Instead, the decrease in intensity suggests less sulfide (S^{2-}) character that can transition to Ti t_{2g} and e_g orbitals and more persulfide-like $[(S_2)^{2-}]$ character in the material. This trend differs from the Fe-substituted Li_2TiS_3 material $Li_{1.13}Ti_{0.57}Fe_{0.3}S_2$ reported by Saha *et al.*, which exhibits an increase in intensity of the t_{2g} and e_g states whose peak positions do not align with the pre-edge peak in TiS_3.[24] Lastly, the shift in peak c is a clear indication that electrons are extracted from the S states. Together, the absence of a peak shift in Ti K-edge XANES and the emergence of the new pre-edge peak in S K-edge XANES of fully charged $LiTi_{0.75}\square_{0.25}S_2$ serve as direct evidence that cation vacancies activate anion oxidation through persulfide formation. We also note that X-ray emission spectroscopy (XES) of $LiTi_{0.75}\square_{0.25}S_2$ reveals a shift in K_α suggesting oxidized S and a new feature in K_β suggesting a new bonding environment that resembles TiS_3, further suggesting S-oxidation through persulfide formation (see Supporting Note 2).

Discussion and Conclusions. Through careful control over the structure and crystal chemistry, we have shown that S^{2-} oxidation requires the presence of cation vacancies. We have shown that Ti can chemically substitute Li in $Li(Li_{1/3}Ti_{2/3})S_2$ and introduce vacancies in the structure, keeping the electronic structure of Ti unchanged at predominantly Ti^{4+}. Galvanostatic cycling data of $Li_{1.33-1.33z}Ti_{0.67+0.33z}\square_zS_2$ reveal that while $Li(Li_{1/3}Ti_{2/3})S_2$ exhibits negligible charge capacity (Figure 4a), its vacancy-containing analogues such as $LiTi_{0.75}\square_{0.25}S_2$ can be substantially oxidized. The origin of this oxidation is electron removal from states with predominantly S p character, since the S^{2-} p and the empty Ti^{4+} d states lie below and above the Fermi level, respectively.[34] Similarly, first-principles calculations suggest that S-oxidation into persulfides is favorable only when it is accompanied by a large degree of lattice contraction near a vacancy.

In all samples, any accessible S-oxidation proceeds *via* a two-phase mechanism with a high degree of disorder in the S sublattice, suggesting distorted S positions. Spectroscopic evidence suggests that Ti does not participate throughout the charge, and all charge compensation stems from S-oxidation. S K-edge XANES shows the growth of an electronic transition associated with the S_2^{2-} persulfide in the fully charged $LiTi_{0.75}\square_{0.25}S_2$, which strongly indicates S-oxidation through the formation of persulfides. It may be possible that lattice anion oxidation occurs during charge and persulfide formation arises during a week-long relaxation period between sample preparation and XANES measurement, but the voltage profile matches the DFT calculations, eliminating this possibility.

The exact mechanism of S-oxidation, whether in the form of persulfides $[(S_2)^{2-}]$ or S^{n-} ($n < 2$), has been debated. Saha *et al.* reported that in $Li_{1.17}Ti_{0.58}Fe_{0.25}S_2$, anion holes are delocalized through Fe−S interaction, and no S−S bond with the bond length of 2.1 Å is observed.[24] Leube *et al.* proposed a complex balance between anion (S^{2-}/S^{n-} and Se^{2-}/Se^{n-}, $n < 2$) and cation ($Ti^{3+/4+}$) redox processes in $Li_2TiS_{3-x}Se_x$.[34] On the other hand, Sakuda *et al.* demonstrated that mechanochemically synthesized rock-salt-like cation-disordered ($Fm\bar{3}m$) Li_2TiS_3 exhibits anion redox, resulting in the formation of S−S bonds along the TiS_6 edge, supported by PDF showing a correlation near 2.0 Å.[31,51] Hansen *et al.* demonstrated that a pre-edge feature associated with pyrite FeS_2 (S_2^{2-}) is observed in S XANES of charged Li_2FeS_2.[44] Also, Wang *et al.* showed that a feature around 2 Å associated with S−S is observed in S EXAFS of layered $NaCr_{2/3}Ti_{1/3}S_2$.[52] In this work, based on first-principles simulations, electrochemical performance, and spectroscopic evidence, we propose that S-oxidation occurs through persulfide formation due to the dependence of anion oxidation on the presence of cation vacancies. The vacancies provide space for the resulting

https://doi.org/10.1021/jacs.4c05769
J. Am. Chem. Soc. 2024, 146, 20951−20962

structural distortions. Additionally, it is likely that vacancies release S p orbitals from M−anion bonding orbitals, allowing for rehybridization to form the new S−S bond. In fact, by evaluating two isostructural sulfides with two metals of very different d band positions, Fe and Co, we find that the anion oxidation plateau voltage is independent of the metal, suggesting that S nonbonding p orbitals are the operative electronic state from which oxidation occurs.[53] Furthermore, we note that similar electronic states have been associated with the origin of anion redox activity in oxides. Li−O−Li configurations have been suggested to release O p orbitals from metal−anion bonding to yield "orphaned," unhybridized O 2p orbitals from which anion oxidation is suggested to occur.[54] However, if Li−anion−Li environments were the enabling structural feature to form the unhybridized, or nonbonding, bands, then the $Li_{1.33-1.33z}Ti_{0.67+0.33z}\square_zS_2$ series should reflect the opposite trend of capacity *vs* vacancy content; fewer vacancies would yield more Li, and thus a higher probability of Li−S−Li environments and higher capacity. Instead, we see that the anion oxidation capacity increases with vacancy content, which would suggest that S p nonbonding bands can only be liberated by cation vacancies. Additionally, it has been suggested that Li_2TiS_3 is inactive due to the unfavorable position of the metal d band that prevents a ligand to metal charge transfer from S^{2-} to Ti^{4+}.[55] However, since we are able to sustain significant anion oxidation capacity in $LiTi_{0.75}\square_{0.25}S_2$, which contains all Ti^{4+}, we suggest that the reason Li_2TiS_3 is inactive is due to the inability of the material to distort to form S−S bonds and the lack of S nonbonding states.

We have shown that in sulfides, vacancies are crucial to allow for S−S bond formation. From calculations, vacancies in the transition metal layer are most important, and experimentally, we demonstrate that formation of vacancies is a prerequisite for persulfide formation. This insight can be extended to oxides where anion redox appears to involve transition metal migration and the formation of trapped O_2^{n-} molecular species that detach from the crystalline network.[10,11,16] Recent works in oxides have suggested that vacancies play an important role in anion redox mechanisms that involve structural modifications.[18,28,29] The model system presented in this work clearly demonstrates that vacancies are essential to enable structure-altering anion redox.

To summarize, we demonstrated that the introduction of vacancies *via* chemical substitution activates anion redox in otherwise electrochemically inert $Li(Li_{1/3}Ti_{2/3})S_2$. By introducing intrinsic vacancies, we can engineer the material on the atomic scale to accommodate structural distortions associated with persulfide formation and activate anion redox. By maintaining the electron configuration of Ti at d^0, we are able to isolate the role of vacancies in activating anion redox and demonstrate that anion redox without transition metal oxidation is possible. This finding offers new insights regarding the origin of anion redox, which involves partial structural transformations.

EXPERIMENTAL SECTION

Material Preparation. All materials were prepared using traditional solid-state methods in an Ar-filled glovebox, in which O_2 and H_2O levels were <1 ppm. The Ti/S ratio of commercially available TiS_2 (Thermo Scientific Chemicals, ≥99.8%) based on EPMA is 1:1.93. Therefore, materials prepared with the commercially available TiS_2 are labeled as "Ti-rich." Stoichiometric TiS_2 was prepared by grinding a 1:2.1 molar ratio of Ti metal powder (325 mesh, Thermo Scientific Chemicals, ≥99.5%) and S (S_8, Acros Organics, >99.5%), which was then pressed into 400 mg pellets and sealed in an evacuated vitreous silica ampule. The reactants were heated at 3 °C min^{-1} to 600 °C with a dwell time of 24 h before being cooled to room temperature. $Li_{1.33-1.33z}Ti_{0.67+0.33z}\square_zS_2$ was prepared by grinding stoichiometric quantities of Li_2S (Beantown Chemical, 99.9%), stoichiometric TiS_2, and 0.1 molar excess S pressed into 300 mg pellets. Pellets were placed inside carbon-coated vitreous silica ampules and heated at 3 °C min^{-1} to 750 °C with a dwell time of 48 h before cooling to room temperature. "Ti-rich" $LiTi_{0.75}\square_{0.25}S_2$ was synthesized by the same procedure, but with stoichiometric quantities of Li_2S and "Ti-rich" TiS_2. $Li_{1+\alpha}Ti_{0.75}\square_{0.25-\alpha}S_2$ was synthesized by the same procedure, but with stoichiometric quantities of Li_2S (Beantown Chemical), stoichiometric TiS_2, Ti, and 0.1 excess S pressed into 300 mg pellets. $Li_{0.83}Mg_{0.25}Ti_{0.67}\square_{0.25}S_2$ was synthesized by the same procedure, but with stoichiometric quantities of Li_2S (Beantown Chemical), stoichiometric TiS_2, Mg powder (Sigma-Aldrich, >99%), S (Acros Organics), and 0.1 excess S (Acros Organics) pressed into 300 mg pellets. The color of all materials synthesized was black.

Electrochemical Characterization. All cells were prepared inside Ar-filled gloveboxes, in which H_2O and O_2 levels were below 0.1 ppm. Active materials of $Li_{1.33-1.33z}Ti_{0.67+0.33z}\square_zS_2$ and $Li_{1+\alpha}Ti_{0.75}\square_{0.25-\alpha}S_2$ were mixed with Super P carbon (Alfa Aesar, ≥99%) and polytetrafluoroethylene (PTFE, Sigma-Aldrich) at a ratio of 3:1:1 by mass to make composite electrodes. The active material and carbon were hand-ground together first for 5 min, and then PTFE was added to the mixture and hand-ground with a mortar and pestle. Approximately 10 mg of the composite mixture was then pressed into 0.25 in. diameter pellets with a hand-operated arbor press. 2032 coin cells were prepared with polished Li metal counter/reference electrodes, dried 18 mm diameter glass fiber separators (Whatman GF/D), and 11 drops of electrolyte (approximately 165 mg). The electrolyte in all cells was a 1 M solution of $LiPF_6$ (Sigma-Aldrich, ≥99.99%) in a 1:1:3 mixture of ethylene carbonate (Sigma-Aldrich, >99%), propylene carbonate (Sigma-Aldrich, >99%), and dimethyl carbonate (Sigma-Aldrich, >99%) by volume. All potentials are in reference to the Li metal counter/reference electrode potential, which is approximated to equal that of Li/Li^+. Galvanostatic cycling data were collected at C/20 based on 1 e^- per formula unit. $LiTi_{0.75}\square_{0.25}S_2$ in a Mg electrolyte system was prepared in a similar manner to a previously reported TiS_2 cathode in a Mg electrolyte.[38] $LiTi_{0.75}\square_{0.25}S_2$ was mixed with Super P carbon (Alfa Aesar, 99%) and poly(vinylidene fluoride) (PVDF, MTI Corp.) at a mass ratio of 8:1:1 in *N*-methyl-2-pyrrolindone (NMP, Thermo Scientific), and the slurry was casted onto Mo foil (Alfa Aesar, >99%). 1/4 in. diameter PTFE Swagelok cells were prepared with polished Mg metal (MTI Corp., >99%) counter/reference electrodes, dried 1/4 in. diameter glass fiber separators (Whatman GF/D), and 5 drops of electrolyte (approximately 56 mg). The electrolyte in all cells was 0.2 M all-phenyl complex (APC) using 1:2 aluminum chloride, anhydrous (Beantown Chemical, >99%):phenylmagnesium chloride (Sigma-Aldrich, 2.0 M in THF) with 10 wt % excess aluminum chloride in THF (Sigma). Galvanostatic cycling data was collected at C/100 based on 1 e^- per formula unit in an oven at 60 °C.

Material Characterization. For powder XRD, the powders were placed on an air-free sample holder (Rigaku) inside the glovebox to prevent air exposure during the measurement. XRD patterns were collected on a Rigaku diffractometer with a Cu Kα X-ray source at 3° min^{-1} with 0.04° step size. The diffraction patterns were fit by the Rietveld method using GSAS-II.[56] Visualization of the crystal structures was aided by VESTA.[57]

High-resolution synchrotron powder XRD patterns were collected on beamline 11-BM-B (λ = 0.458979 Å) at the Advanced Photon Source at Argonne National Laboratory.[58] The powder of $LiTi_{0.75}\square_{0.25}S_2$ was used for the pristine state, while the *ex situ* charged sample was prepared using 16 mg of a 60:20:20 wt % pellet consisting of active material, Super P carbon, and PTFE. A cell fully charged to 3 V was disassembled in an Ar-filled glovebox, and the cathode composite was recovered from the disassembled cell, washed

https://doi.org/10.1021/jacs.4c05769
J. Am. Chem. Soc. 2024, 146, 20951−20962

with 200 μL of dimethyl carbonate, and vacuum-dried. The sample was sealed under vacuum in 0.7 mm (O.D.) glass capillaries (Hampton Research) to prevent air exposure and placed inside polyimide capillaries.

Operando XRD data were collected using a Bruker D8 Advance diffractometer in Bragg−Brentano geometry equipped with a Cu Kα source (λ_1 = 1.5406 Å, λ_2 = 1.5444 Å) and a LYNXEYE XE-T detector. A custom-made *operando* cell with a PEEK body, stainless steel electrical contacts, and an X-ray-transparent Be window (SPI Supplies, 0.25 mm thick) was used. The Be window served as a current collector and allowed for X-ray penetration, so that diffraction patterns could be collected while cycling galvanostatically. As with the *ex situ* cells, pellet electrodes composed of 60% active material, 20% carbon black, and 20% polymer binder were used and placed directly in the Be window. The pellet electrodes were cycled against Li foil using a BioLogic SP-200 potentiostat at a C/20 rate with one Whatman glass fiber separator (GF/D) flooded with 1 M $LiPF_6$ in a 1:1:1 EC/PC/DMC electrolyte. Patterns were continuously collected over a range of 10 to 45° 2θ approximately every 20 min throughout the duration of the electrochemical cycling.

TEM imaging was conducted using a Thermo Fisher Talos F200X G2 S/TEM at an accelerating voltage of 200 keV under high-resolution TEM (HRTEM) mode. TEM samples of pristine $LiTi_{0.75}\square_{0.25}S_2$ and charged $LiTi_{0.75}\square_{0.25}S_2$ were prepared through dry transfer powders onto 200 mesh lacey carbon films on copper grids (Ted Pella, Inc.). The fast Fourier transformation (FFT) pattern simulation from the HRTEM image of pristine $LiTi_{0.75}\square_{0.25}S_2$ was performed in ImageJ and was matched to [110] zone axis by CrysTBox diffractGUI.[59]

EPMA was conducted using a JEOL JXA-8200 with a 10 kV and 5 nA focused beam. The focused electron beam is 150 nm in diameter. Standards for analysis were TiO_2 for Ti and FeS_2 for S. 30 mg of powder was pressed with a hydraulic press for 5 min at 2 tons inside an Ar-filled glovebox. C was sputtered onto the pellets using graphite under vacuum and transferred to the instrument. There was <30 s of air exposure during transfer. Seven different areas were selected and measured.

ICP−MS was performed on an Agilent 8800. Three replicates of 3−4 mg of $LiTi_{0.75}\square_{0.25}S_2$ were dissolved in 5% nitic acid solution at 60 °C for 2 h. Upon dissolution, the solutions were diluted twice in 5% nitric acid to reach ×2500 dilution. Five different concentrations were chosen as standards from 100.02 ppm of Ti and 998 ppm of Li standard solutions.

ssNMR was performed using a Bruker AVANCE 500 MHz spectrometer operating at 194.31 MHz for ^{7}Li. All samples were packed in a 4 mm ZrO_2 HR-MAS rotor with a 50 μL PTFE spacer (CortecNet). 40 mg of pristine powders of $Li(Li_{1/3}Ti_{2/3})S_2$ and $LiTi_{0.75}\square_{0.25}S_2$ were packed into the rotor in an Ar-filled glovebox. *Ex situ* samples were prepared in the same way as electrochemical cells in coin cells, with a total mass of 20 mg. Upon reaching the appropriate state of charge, the cathode composite was recovered and washed with 300 μL of dimethyl carbonate and vacuum-dried in an Ar-filled glovebox. ^{6}Li and ^{7}Li MAS ssNMR were recorded spinning at 13 kHz. A single RF pulse of 0.5 μs with 4 μs $\pi/2$ was applied. The ^{7}Li MAS spectra were fit with DMFIT by using Quasar. The $Li(Li_{1/3}Ti_{2/3})S_2$ spectrum was fit while fixing the relative areas of the peaks at 50:25:25%. ^{6}Li and ^{7}Li spectra were referenced by using LiCl as the standard at 0 ppm.

EPR spectroscopy data were collected with a Bruker EMX X-band CW-EPR spectrometer operating at 9.4 GHz. In an Ar-filled glovebox, 30 mg of powder was packed into a 1.8 mm O.D. quartz capillary, which was then placed inside an EPR tube and sealed with a septum to prevent air exposure. The tube was placed in LN_2 Dewar flask during measurement. Spectra were acquired with a microwave power of 2.185 mW and an amplitude modulation of 8 G.

Ti XAS was conducted at beamline 2-2 at the Stanford Synchrotron Radiation Lightsource at the SLAC National Accelerator Laboratory. Data processing including calibration and background correction was performed using Athena.[60] The Ti K-edge data were calibrated to collinear Ti foil for each sample. *Ex situ* samples were prepared in the same way as electrochemical cells in coin cells, with a total mass of 20 mg. Upon reaching the appropriate state of charge, the cathode composite was recovered and washed with 300 μL of dimethyl carbonate and vacuum-dried in an Ar-filled glovebox. *Ex situ* samples were placed onto the sample holder by using Kapton tape on each side inside an Ar-filled glovebox. During measurement, the sample holder was placed in a continuous He-flushed chamber with minimal O_2 concentration (<500 ppm). Each scan lasted about 15 min, and 3 scans were averaged.

S K-edge XAS was conducted at beamline 8-BM at the National Synchrotron Light Source II at Brookhaven National Laboratory. The S K-edge data were calibrated to a gypsum standard. *Ex situ* samples were prepared by grinding cycled cathode material with boron nitride to achieve 5 wt % S concentrations. Pellets were then sandwiched between a polypropylene layer and Kapton tape and adhered to the sample holder by using Kapton tape. All sample preparation was conducted inside an Ar-filled glovebox. During measurement, the sample holder was placed in a continuous He-flushed chamber to minimize air exposure. Each scan lasted about 15 min, and 3 scans were averaged.

S XES was performed by using the Brimstone laboratory spectrometer (easyXAFS LLC, Renton, WA, USA). The spectrometer utilized a Pd-anode X-ray tube and was operated at 24 kV and 3 mA. The spectrometer uses the easyXAFS Kromo cmos-based position-sensitive energy resolving detector. Using a Si(111) crystal analyzer with a radius of curvature of 100 mm, the S K_α spectra were measured at a Bragg angle of 59.0°, and S K_β spectra were measured at a Bragg angle of 53.4°. To reduce Johann error for optimal resolution, the 20 mm wide analyzer was masked to use only the central 4 mm. Measurements were performed under helium flushed into the experimental chamber at atmospheric pressure. Samples were prepared by encapsulating the powder samples between a lower layer of Kapton tape and an upper layer of 8 μm thick Kapton film. The sealed samples were then briefly exposed to air during mounting into the spectrometer (15 min) and during the helium flushing (25 min). Some residual air is expected to remain in the chamber, even after flushing. Samples were mounted on an automatic sample changer, and a series of repeated short scans (3 min each) were measured alternately between each sample and reference compounds, and 5 scans were averaged. Resulting data were monitored for possible changes due to instrumental drift or changes in sample signal over time from radiation damage, air exposure, or other effects. ZnS and Na_2SO_4 were used as standards for calibration, and the spectra are shown in Figure S22.

Computational Methods. DFT calculations were performed using the Vienna *ab initio* simulation package (VASP),[61] following the protocol recently benchmarked specifically for capturing the behavior of mixed metal-centric and anion-centric redox processes.[8,11] Specifically, we rely on the SCAN exchange−correlation functional[62] and projector-augmented wave method,[63] Gaussian smearing (σ = 0.05 eV), and a reciprocal space discretization of 25 k-points per Å^{-1}. All calculations were converged to 10^{-5} eV in total energy and 20 meV Å^{-1} in forces. No specific symmetry was assumed or enforced, and no further corrections were used. Energies were optimized over all distinct combinations of Li-vacancy configurations, together with zero, one, or two S_2 dimers per Ti-vacancy. In the enumeration, we account for both standard octahedral Li sites and tetrahedral Li configurations reported in analogous systems.[64] Configurational enumeration was limited to 1 unit cell, as shown in Figure 2a, that is, considering up to 10 total Li and 1 vacancy in the Ti layer. Structural enumeration and calculation post-processing was performed using the pymatgen Python package.[65]

■ ASSOCIATED CONTENT

Supporting Information

The Supporting Information is available free of charge at https://pubs.acs.org/doi/10.1021/jacs.4c05769.

XRD patterns of $Li_{1.33-1.33z}Ti_{0.67+0.33z}\square_zS_2$; sXRD patterns of $LiTi_{0.75}\square_{0.25}S_2$; Rietveld refinement of

https://doi.org/10.1021/jacs.4c05769
J. Am. Chem. Soc. 2024, 146, 20951−20962

pristine $LiTi_{0.75}\square_{0.25}S_2$; HRTEM image of pristine $LiTi_{0.75}\square_{0.25}S_2$; Rietveld refinement of charged $LiTi_{0.75}\square_{0.25}S_2$; galvanostatic discharge curves of $LiTi_{0.75}\square_{0.25}S_2$ at 60 °C and C/100; ^{6}Li and ^{7}Li MAS ssNMR spectra of $Li_{1.33-1.33z}Ti_{0.67+0.33z}\square_zS_2$; MAS ^{7}Li ssNMR spectrum of $LiTi_{0.75}\square_{0.25}S_2$; DFT enumerations of pristine structure; static ^{7}Li ssNMR spectra of $LiTi_{0.75}\square_{0.25}S_2$; ^{7}Li MAS ssNMR spectrum of $LiTi_{0.75}\square_{0.25}S_2$ at 10 kHz in a 4.7 T spectrometer; EPR spectra of $Li_{1.33}Ti_{0.67}S_2$ and $LiTi_{0.75}\square_{0.25}S_2$; GITT of $Li_{1.33}Ti_{0.67}S_2$; XRD patterns of $Li_{1+\alpha}Ti_{0.75}\square_{0.25-\alpha}S_2$; first charge and discharge curves of $Li_{1+\alpha}Ti_{0.75}\square_{0.25-\alpha}S_2$; galvanostatic cycling data of $LiTi_{0.75}\square_{0.25}S_2$ discharged first; XRD patterns of $Li_{0.83}Ti_{0.67}Mg_{0.25}\square_{0.25}S_2$; *operando* XRD patterns of $LiTi_{0.75}\square_{0.25}S_2$; simulated XRD patterns of $LiTi_{0.75}\square_{0.25}S_2$; ^{7}Li MAS ssNMR spectrum of fully charged $LiTi_{0.75}\square_{0.25}S_2$; Ti XANES spectra of $LiTiS_2$, $Li_{1.33}Ti_{0.67}S_2$, $LiTi_{0.75}\square_{0.25}S_2$, and TiS_2; S K_α XES spectra of ZnS and Na_2SO_4; and polarization of $Li_{1.33}Ti_{0.67}S_2$ cycled to higher V cutoff (PDF)

AUTHOR INFORMATION

Corresponding Author

Kimberly A. See − *Division of Chemistry and Chemical Engineering, California Institute of Technology, Pasadena, California 91125, United States;* orcid.org/0000-0002-0133-9693; Email: ksee@caltech.edu

Authors

Seong Shik Kim − *Division of Chemistry and Chemical Engineering, California Institute of Technology, Pasadena, California 91125, United States;* orcid.org/0000-0003-2604-6392

Daniil A. Kitchaev − *Materials Department, University of California, Santa Barbara, California 93106, United States*

Eshaan S. Patheria − *Division of Chemistry and Chemical Engineering, California Institute of Technology, Pasadena, California 91125, United States;* orcid.org/0000-0002-2761-8498

Colin T. Morrell − *Division of Chemistry and Chemical Engineering, California Institute of Technology, Pasadena, California 91125, United States;* orcid.org/0000-0002-8010-2474

Michelle D. Qian − *Division of Chemistry and Chemical Engineering, California Institute of Technology, Pasadena, California 91125, United States;* orcid.org/0000-0002-4815-1014

Jessica L. Andrews − *Department of Chemistry, University of Southern California, Los Angeles, California 90089, United States*

Qizhang Yan − *Department of NanoEngineering, University of California San Deigo, La Jolla, California 92093, United States*

Shu-Ting Ko − *Materials Science and Engineering Program, University of California San Deigo, La Jolla, California 92093, United States*

Jian Luo − *Department of NanoEngineering, University of California San Deigo, La Jolla, California 92093, United States*

Brent C. Melot − *Department of Chemistry, University of Southern California, Los Angeles, California 90089, United States; Department of Chemical Engineering and Materials Science, University of Southern California, Los Angeles, California 90089, United States;* orcid.org/0000-0002-7078-8206

Anton Van der Ven − *Materials Department, University of California, Santa Barbara, California 93106, United States*

Complete contact information is available at: https://pubs.acs.org/10.1021/jacs.4c05769

Notes

The authors declare no competing financial interest.

ACKNOWLEDGMENTS

This work was supported by the Center for Synthetic Control across Length-Scales for Advancing Rechargeables (SCALAR), an Energy Frontier Research Center funded by the U.S. Department of Energy, Office of Science, Basic Energy Sciences under award no. DE-SC0019381. K.A.S. acknowledges support from the David and Lucile Packard Foundation. Use of the Stanford Synchrotron Radiation Lightsource, SLAC National Accelerator Laboratory, is supported by the U.S. Department of Energy, Office of Science, Office of Basic Energy Sciences under contract no. DE-AC02-76SF00515. Use of the Advanced Photon Source at Argonne National Laboratory was supported by the U.S. Department of Energy, Office of Science, Office of Basic Energy Sciences under contract no. DE-AC02-06CH11357. This research used 8-BM of the National Synchrotron Light Source II, a U.S. Department of Energy (DOE) Office of Science User Facility operated for the DOE Office of Science by Brookhaven National Laboratory under contract no. DE-SC0012704. This project benefited from the use of instrumentation made available by the Resnick Sustainability Institute's Water and Environment Lab at the California Institute of Technology. M.D.Q. acknowledges support from the National Science Foundation Graduate Research Fellowship under grant no. DGE1745301. J.L.A. acknowledges support from the National Science Foundation Graduate Research Fellowship Program under grant no. DGE-1842487. We thank Dr. Sonjong Hwang (solid-state NMR), Dr. Paul Oyala (electron paramagnetic resonance), Dr. William Holden at easyXAFS (X-ray emission spectroscopy) for technical assistance and/or helpful discussions.

REFERENCES

(1) Whittingham, M. S. Lithium Batteries: 50 Years of advances to address the next 20 years of climate issues. *Nano Lett.* **2020**, *20*, 8435−8437.

(2) Chen, T.; Jin, Y.; Lv, H.; Yang, A.; Liu, M.; Chen, B.; Xie, Y.; Chen, Q. Applications of lithium-ion batteries in grid-scale energy storage systems. *Trans. Tianjin Univ.* **2020**, *26*, 208−217.

(3) Genreith-Schriever, A. R.; Banerjee, H.; Menon, A. S.; Bassey, E. N.; Piper, L. F. J.; Grey, C. P.; Morris, A. J. Oxygen Hole Formation Controls Stability in $LiNiO_2$ Cathodes. *Joule* **2023**, *7*, 1623−1640.

(4) Mizokawa, T.; Wakisaka, Y.; Sudayama, T.; Iwai, C.; Miyoshi, K.; Takeuchi, J.; Wadati, H.; Hawthorn, D. G.; Regier, T. Z.; Sawatzky, G. A. Role of Oxygen Holes in Li_xCoO_2 Revealed by Soft X-Ray Spectroscopy. *Phys. Rev. Lett.* **2013**, *111*, 056404.

(5) Radin, M. D.; Hy, S.; Sina, M.; Fang, C.; Liu, H.; Vinckeviciute, J.; Zhang, M.; Whittingham, M. S.; Meng, Y. S.; Van der Ven, A. Narrowing the gap between theoretical and practical capacities in Li-ion layered oxide cathode materials. *Adv. Energy Mater.* **2017**, *7*, 1602888.

(6) Assat, G.; Tarascon, J.-M. Fundamental understanding and practical challenges of anionic redox activity in Li-ion batteries. *Nat. Energy* **2018**, *3*, 373−386.

(7) Zhang, M.; Kitchaev, D. A.; Lebens-Higgins, Z.; Vinckeviciute, J.; Zuba, M.; Reeves, P. J.; Grey, C. P.; Whittingham, M. S.; Piper, L. F. J.; Van der Ven, A.; Meng, Y. S. Pushing the limit of 3d transition metal-based layered oxides that use both cation and anion redox for energy storage. *Nat. Rev. Mater.* **2022**, *7*, 522−540.
(8) Kitchaev, D. A.; Vinckeviciute, J.; Van der Ven, A. Delocalized metal−oxygen π-redox is the origin of anomalous nonhysteretic capacity in Li-ion and Na-ion cathode materials. *J. Am. Chem. Soc.* **2021**, *143*, 1908−1916.
(9) Sudayama, T.; Uehara, K.; Mukai, T.; Asakura, D.; Shi, X.-M.; Tsuchimoto, A.; Mortemard de Boisse, B.; Shimada, T.; Watanabe, E.; Harada, Y.; Nakayama, M.; Okubo, M.; Yamada, A. Multiorbital bond formation for stable oxygen-redox reaction in battery electrodes. *Energy Environ. Sci.* **2020**, *13*, 1492−1500.
(10) Radin, M. D.; Vinckeviciute, J.; Seshadri, R.; Van der Ven, A. Manganese oxidation as the origin of the anomalous capacity of Mn-containing Li-excess cathode materials. *Nat. Energy* **2019**, *4*, 639−646.
(11) Vinckeviciute, J.; Kitchaev, D. A.; Van der Ven, A. A Two-step oxidation mechanism controlled by Mn migration explains the first-cycle activation behavior of Li_2MnO_3-based Li-excess materials. *Chem. Mater.* **2021**, *33*, 1625−1636.
(12) Sathiya, M.; Rousse, G.; Ramesha, K.; Laisa, C. P.; Vezin, H.; Sougrati, M. T.; Doublet, M.-L.; Foix, D.; Gonbeau, D.; Walker, W.; Prakash, A. S.; Ben Hassine, M.; Dupont, L.; Tarascon, J.-M. Reversible anionic redox chemistry in high-capacity layered-oxide electrodes. *Nat. Mater.* **2013**, *12*, 827−835.
(13) Li, X.; Qiao, Y.; Guo, S.; Xu, Z.; Zhu, H.; Zhang, X.; Yuan, Y.; He, P.; Ishida, M.; Zhou, H. Direct visualization of the reversible O^{2-}/O^- redox process in Li-rich cathode materials. *Adv. Mater.* **2018**, *30*, 1705197.
(14) McCalla, E.; Abakumov, A. M.; Saubanère, M.; Foix, D.; Berg, E. J.; Rousse, G.; Doublet, M.-L.; Gonbeau, D.; Novák, P.; Van Tendeloo, G.; Dominko, R.; Tarascon, J.-M. Visualization of O−O peroxo-like dimers in high-capacity layered oxides for Li-ion batteries. *Science* **2015**, *350*, 1516−1521.
(15) Chen, H.; Islam, M. S. Lithium extraction mechanism in Li-rich Li_2MnO_3 involving oxygen hole formation and dimerization. *Chem. Mater.* **2016**, *28*, 6656−6663.
(16) House, R. A.; Rees, G. J.; Perez-Osorio, M. A.; Marie, J.-J.; Boivin, E.; Robertson, A. W.; Nag, A.; Garcia-Fernandez, M.; Zhou, K.-J.; Bruce, P. G. First-cycle voltage hysteresis in Li-rich 3d cathodes associated with molecular O_2 trapped in the bulk. *Nat. Energy* **2020**, *5*, 777−785.
(17) Kaufman, L. A.; McCloskey, B. D. Surface Lithium carbonate influences electrolyte degradation via reactive oxygen attack in Lithium-excess cathode materials. *Chem. Mater.* **2021**, *33*, 4170−4176.
(18) House, R. A.; Rees, G. J.; McColl, K.; Marie, J.-J.; Garcia-Fernandez, M.; Nag, A.; Zhou, K.-J.; Cassidy, S.; Morgan, B. J.; Saiful Islam, M.; Bruce, P. G. Delocalized Electron Holes on Oxygen in a Battery Cathode. *Nat. Energy* **2023**, *8*, 351−360.
(19) Renfrew, S. E.; McCloskey, B. D. Quantification of surface oxygen depletion and solid carbonate evolution on the first cycle of $LiNi_{0.6}Mn_{0.2}Co_{0.2}O_2$ Electrodes. *ACS Appl. Energy Mater.* **2019**, *2*, 3762−3772.
(20) Gent, W. E.; Lim, K.; Liang, Y.; Li, Q.; Barnes, T.; Ahn, S.-J.; Stone, K. H.; McIntire, M.; Hong, J.; Song, J. H.; et al. Coupling between oxygen redox and cation migration explains unusual electrochemistry in Lithium-rich layered oxides. *Nat. Commun.* **2017**, *8*, 2091.
(21) Hu, E.; Yu, X.; Lin, R.; Bi, X.; Lu, J.; Bak, S.; Nam, K.-W.; Xin, H. L.; Jaye, C.; Fischer, D. A.; Amine, K.; Yang, X.-Q. Evolution of redox couples in Li- and Mn-rich cathode materials and mitigation of voltage fade by reducing oxygen release. *Nat. Energy* **2018**, *3*, 690−698.
(22) Rana, J.; Papp, J. K.; Lebens-Higgins, Z.; Zuba, M.; Kaufman, L. A.; Goel, A.; Schmuch, R.; Winter, M.; Whittingham, M. S.; Yang, W.; McCloskey, B. D.; Piper, L. F. J. Quantifying the capacity contributions during activation of Li_2MnO_3. *ACS Energy Lett.* **2020**, *5*, 634−641.
(23) Zak, J. J.; Kim, S. S.; Laskowski, F. A. L.; See, K. A. An Exploration of sulfur redox in lithium battery cathodes. *J. Am. Chem. Soc.* **2022**, *144*, 10119−10132.
(24) Saha, S.; Assat, G.; Sougrati, M. T.; Foix, D.; Li, H.; Vergnet, J.; Turi, S.; Ha, Y.; Yang, W.; Cabana, J.; Rousse, G.; Abakumov, A. M.; Tarascon, J.-M. Exploring the bottlenecks of anionic redox in Li-rich layered sulfides. *Nat. Energy* **2019**, *4*, 977−987.
(25) Murphy, D. W.; Trumbore, F. A. The Chemistry of TiS3 and NbSe3 Cathodes. *J. Electrochem. Soc.* **1976**, *123*, 960−964.
(26) Rouxel, J. Anion−Cation Redox Competition and the Formation of New Compounds in Highly Covalent Systems. *Chem.—Eur. J.* **1996**, *2*, 1053−1059.
(27) Whittingham, M. Chemistry of Intercalation Compounds: Metal Guests in Chalcogenide Hosts. *Prog. Solid State Chem.* **1978**, *12*, 41−99.
(28) Hong, J.; Gent, W. E.; Xiao, P.; Lim, K.; Seo, D.; Wu, J.; Csernica, P. M.; Takacs, C. J.; Nordlund, D.; Sun, C.; Stone, K. H.; Passarello, D.; Yang, W.; Prendergast, D.; Ceder, G.; Toney, M.; Chueh, W. C. Metal−Oxygen decoordination stabilizes anion redox in Li-rich oxides. *Nat. Mater.* **2019**, *18*, 256−265.
(29) House, R. A.; Maitra, U.; Pérez-Osorio, M. A.; Lozano, J. G.; Jin, L.; Somerville, J. W.; Duda, L. C.; Nag, A.; Walters, A.; Zhou, K.-J.; Roberts, M. R.; Bruce, P. G. Superstructure Control of First-Cycle Voltage Hysteresis in Oxygen-Redox Cathodes. *Nature* **2020**, *577*, 502−508.
(30) Fleet, M.; Harmer, S.; Liu, X.; Nesbitt, H. Polarized X-ray Absorption Spectroscopy and XPS of TiS_3: S K-and Ti L-edge XANES and S and Ti 2p XPS. *Surf. Sci.* **2005**, *584*, 133−145.
(31) Sakuda, A.; Takeuchi, T.; Okamura, K.; Kobayashi, H.; Sakaebe, H.; Tatsumi, K.; Ogumi, Z. Rock-salt-type lithium metal sulphides as novel positive-electrode materials. *Sci. Rep.* **2014**, *4*, 4883.
(32) Li, B.; Jiang, N.; Huang, W.; Yan, H.; Zuo, Y.; Xia, D. *Studies on Anionic Redox in Li-Rich Cathode Materials of Li-Ion Batteries*; Springer Singapore: Singapore, 2019; pp 99−121.
(33) Flamary-Mespoulie, F.; Boulineau, A.; Martinez, H.; Suchomel, M. R.; Delmas, C.; Pecquenard, B.; Le Cras, F. Lithium-rich layered titanium sulfides: Cobalt- and Nickel-free high capacity cathode materials for lithium-ion batteries. *Energy Storage Mater.* **2020**, *26*, 213−222.
(34) Leube, B. T.; Robert, C.; Foix, D.; Porcheron, B.; Dedryvère, R.; Rousse, G.; Salager, E.; Cabelguen, P.-E.; Abakumov, A. M.; Vezin, H.; Doublet, M.-L.; Tarascon, J.-M. Activation of anionic redox in D^0 transition metal chalcogenides by anion doping. *Nat. Commun.* **2021**, *12*, 5485.
(35) Leube, B. T.; Salager, E.; Chesneau, E.; Rousse, G.; Vezin, H.; Abakumov, A. M.; Tarascon, J.-M. Layered sodium titanium trichalcogenide Na_2TiCh_3 framework (Ch = S, Se): A rich crystal and electrochemical chemistry. *Chem. Mater.* **2022**, *34*, 2382−2392.
(36) Llovet, X.; Moy, A.; Pinard, P. T.; Fournelle, J. H. Electron probe microanalysis: A review of recent developments and applications in materials science and engineering. *Prog. Mater. Sci.* **2021**, *116*, 100673.
(37) Lavrent'ev, Y. G.; Karmanov, N. S.; Usova, L. V. Electron probe microanalysis of minerals: microanalyzer or scanning electron microscope? *Russ. Geol. Geophys.* **2015**, *56*, 1154−1161.
(38) Sun, X.; Bonnick, P.; Nazar, L. F. Layered TiS_2 positive electrode for Mg batteries. *ACS Energy Lett.* **2016**, *1*, 297−301.
(39) Baklanova, Y. V.; Arapova, I. Y.; Shein, I. R.; Maksimova, L. G.; Mikhalev, K. N.; Denisova, T. A. Charge distribution and mobility of lithium ions in Li_2TiO_3 from ^{6,7}Li NMR data. *J. Struct. Chem.* **2013**, *54*, 111−118.
(40) Vijayakumar, M.; Kerisit, S.; Yang, Z.; Graff, G. L.; Liu, J.; Sears, J. A.; Burton, S. D.; Rosso, K. M.; Hu, J. Combined ^{6,7}Li NMR and molecular dynamics study of Li diffusion in Li_2TiO_3. *J. Phys. Chem. C* **2009**, *113*, 20108−20116.
(41) Li, L.; Qin, Z.; Ries, L.; Hong, S.; Michel, T.; Yang, J.; Salameh, C.; Bechelany, M.; Miele, P.; Kaplan, D.; Chhowalla, M.; Voiry, D.

https://doi.org/10.1021/jacs.4c05769
J. Am. Chem. Soc. 2024, 146, 20951−20962

Role of sulfur vacancies and undercoordinated Mo regions in MoS_2 nanosheets toward the evolution of hydrogen. *ACS Nano* **2019**, *13*, 6824−6834.
(42) Carter, E.; Carley, A. F.; Murphy, D. M. Evidence for O 2-radical stabilization at surface oxygen vacancies on polycrystalline TiO_2. *J. Phys. Chem. C* **2007**, *111*, 10630−10638.
(43) Nakamura, I.; Negishi, N.; Kutsuna, S.; Ihara, T.; Sugihara, S.; Takeuchi, K. Role of oxygen vacancy in the plasma-treated TiO_2 photocatalyst with visible light activity for NO removal. *J. Mol. Catal. A: Chem.* **2000**, *161*, 205−212.
(44) Hansen, C. J.; Zak, J. J.; Martinolich, A. J.; Ko, J. S.; Bashian, N. H.; Kaboudvand, F.; Van der Ven, A.; Melot, B. C.; Nelson Weker, J.; See, K. A. Multielectron, cation and anion redox in Lithium-rich iron sulfide cathodes. *J. Am. Chem. Soc.* **2020**, *142*, 6737−6749.
(45) Martinolich, A. J.; Zak, J. J.; Agyeman-Budu, D. N.; Kim, S. S.; Bashian, N. H.; Irshad, A.; Narayan, S. R.; Melot, B. C.; Nelson Weker, J.; See, K. A. Controlling covalency and anion redox potentials through anion substitution in Li-rich chalcogenides. *Chem. Mater.* **2021**, *33*, 378−391.
(46) Wu, Z. Y.; Ouvrard, G.; Moreau, P.; Natoli, C. R. Interpretation of preedge features in the Ti and S K-edge x-ray-absorption near-edge spectrain the layered disulfides TiS_2 and TaS_2. *Phys. Rev. B: Condens. Matter Mater. Phys.* **1997**, *55*, 9508−9513.
(47) Zhang, L.; Sun, D.; Kang, J.; Wang, H.-T.; Hsieh, S.-H.; Pong, W.-F.; Bechtel, H. A.; Feng, J.; Wang, L.-W.; Cairns, E. J.; Guo, J. Tracking the Chemical and Structural Evolution of the TiS_2 Electrode in the Lithium-Ion Cell Using Operando X-ray Absorption Spectroscopy. *Nano Lett.* **2018**, *18*, 4506−4515.
(48) Moreau, P.; Ouvrard, G.; Gressier, P.; Ganal, P.; Rouxel, J. Electronic Structures and Charge Transfer in Lithium and Mercury Intercalated Titanium Disulfides. *J. Phys. Chem. Solids* **1996**, *57*, 1117−1122.
(49) Wu, Z. Y.; Ouvrard, G.; Lemaux, S.; Moreau, P.; Gressier, P.; Lemoigno, F.; Rouxel, J. Sulfur K-edge X-ray Absorption Study of the Charge Transfer upon Lithium Intercalation into Titanium Disulfide. *Phys. Rev. Lett.* **1996**, *77*, 2101−2104.
(50) Kravtsova, A. N.; Stekhin, I. E.; Soldatov, A. V.; Liu, X.; Fleet, M. E. Electronic Structure of MS (M = Ca, Mg, Fe, Mn): X-ray Absorption Analysis. *Phys. Rev. B: Condens. Matter Mater. Phys.* **2004**, *69*, 134109.
(51) Sakuda, A. A reversible rocksalt to amorphous phase transition involving anion redox. *Sci. Rep.* **2018**, *8*, 15086.
(52) Wang, T.; Ren, G.-X.; Shadike, Z.; Yue, J.-L.; Cao, M.-H.; Zhang, J.-N.; Chen, M.-W.; Yang, X.-Q.; Bak, S.-M.; Northrup, P.; Liu, P.; Liu, X.-S.; Fu, Z.-W. Anionic redox reaction in layered $NaCr_{2/3}Ti_{1/3}S_2$ through electron holes formation and dimerization of S−S. *Nat. Commun.* **2019**, *10*, 4458.
(53) Kim, S. S.; Agyeman-Budu, D. N.; Zak, J. J.; Andrews, J. L.; Li, J.; Melot, B. C.; Nelson Weker, J.; See, K. A. Effect of Metal d Band Position on Anion Redox in Alkali-Rich Sulfides. *Chem. Mater.* **2024**, *36*, 6454−6463.
(54) Seo, D.-H.; Lee, J.; Urban, A.; Malik, R.; Kang, S.; Ceder, G. The structural and chemical origin of the oxygen redox activity in layered and cation-disordered Li-excess cathode materials. *Nat. Chem.* **2016**, *8*, 692−697.
(55) Li, B.; Jiang, N.; Huang, W.; Yan, H.; Zuo, Y.; Xia, D. Thermodynamic Activation of Charge Transfer in Anionic Redox Process for Li-Ion Batteries. *Adv. Funct. Mater.* **2018**, *28*, 1704864.
(56) Toby, B. H.; Von Dreele, R. B. *GSAS-II*: the genesis of a modern open-source all purpose crystallography software package. *J. Appl. Crystallogr.* **2013**, *46*, 544−549.
(57) Momma, K.; Izumi, F. VESTA 3 for three-dimensional visualization of crystal, volumetric and morphology data. *J. Appl. Crystallogr.* **2011**, *44*, 1272−1276.
(58) Wang, J.; Toby, B. H.; Lee, P. L.; Ribaud, L.; Antao, S. M.; Kurtz, C.; Ramanathan, M.; Von Dreele, R. B.; Beno, M. A. A dedicated powder diffraction beamline at the Advanced Photon Source: commissioning and early operational results. *Rev. Sci. Instrum.* **2008**, *79*, 085105.
(59) Klinger, M. More features, more tools, more *CrysTBox*. *J. Appl. Crystallogr.* **2017**, *50*, 1226−1234.
(60) Ravel, B.; Newville, M. ATHENA, ARTEMIS, HEPHAESTUS Data analysis for X-ray absorption spectroscopy using IFEFFIT. *J. Synchrotron Radiat.* **2005**, *12*, 537−541.
(61) Kresse, G.; Furthmüller, J. Efficiency of ab-initio total energy calculations for metals and semiconductors using a plane-wave basis set. *Comput. Mater. Sci.* **1996**, *6*, 15−50.
(62) Sun, J.; Ruzsinszky, A.; Perdew, J. P. Strongly constrained and appropriately normed semilocal density functional. *Phys. Rev. Lett.* **2015**, *115*, 036402.
(63) Kresse, G.; Joubert, D. From ultrasoft pseudopotentials to the projector augmented-wave method. *Phys. Rev. B: Condens. Matter Mater. Phys.* **1999**, *59*, 1758−1775.
(64) Van der Ven, A.; Bhattacharya, J.; Belak, A. A. Understanding Li diffusion in Li-intercalation compounds. *Acc. Chem. Res.* **2013**, *46*, 1216−1225.
(65) Ong, S. P.; Richards, W. D.; Jain, A.; Hautier, G.; Kocher, M.; Cholia, S.; Gunter, D.; Chevrier, V. L.; Persson, K. A.; Ceder, G. Python Materials Genomics (pymatgen): A robust, open-source python library for materials analysis. *Comput. Mater. Sci.* **2013**, *68*, 314−319.

https://doi.org/10.1021/jacs.4c05769
J. Am. Chem. Soc. 2024, 146, 20951−20962